Photo-induced Ferroelectric Switching in Perovskite $CH_3NH_3PbI_3$ Films

Supplementary Information

Peiqi Wang [1], Jinjin Zhao [1,2,3][1], Liyu Wei [2], Qingfeng Zhu [4], Shuhong Xie [3,4], Jinxi Liu [2],
Xiangjian Meng [5], Jiangyu Li [1,3,*]

1. Department of Mechanical Engineering, University of Washington, Seattle, WA 98195-2600, USA
2. School of Materials Science and Engineering, and Department of Engineering Mechanics, Shijiazhuang Tiedao University, Shijiazhuang, 050043, China
3. Shenzhen Key Laboratory of Nanobiomechanics, Shenzhen Institutes of Advanced Technology, Chinese Academy of Sciences, Shenzhen 518055, Guangdong, China
4. Key Laboratory of Low Dimensional Materials and Application Technology of Ministry of Education, School of Materials Science and Engineering, Xiangtan University, Xiangtan 411105, Hunan, China
5. National Laboratory for Infrared Physics, Shanghai Institute of Technical Physics, Chinese Academy of Sciences, Shanghai 200083, China

Microstructure and device performance. Dense films with granular structure can be seen from the SEM images of $CH_3NH_3PbI_3$ deposited on FTO/TiO_2 and FTO/PEDOTS:PSS substrates, as shown in Fig. S1(a, b), and there is no apparent difference in microstructure induced by different substrates. The XRD spectra of the films are shown in Fig. S1(c), and the peaks, showing preferred (110)-orientation, correspond to crystalline form of perovskite $CH_3NH_3PbI_3$ that match closely with what were reported in literatures[1, 2]. The J-V curves of the PEDOTS:PSS-based p-i-n and TiO_2-based n-i-p types of solar cells are compared in Fig. S1(d), and their key photovoltaic properties are listed in Table S1, obtained under both forward and reverse scanning directions using a relatively slow sweep rate of 0.1V/s. It is observed that n-i-p type cell has a photovoltaic conversion efficiency (PCE) of 14.6% in reverse scan, while p-i-n type cell shows a corresponding PCE of 10.4%, and the hysteresis for both devices are small.

---

[1] Authors to whom the correspondence should be addressed to; jinjinzhao2012@163.com and jjli@uw.edu.

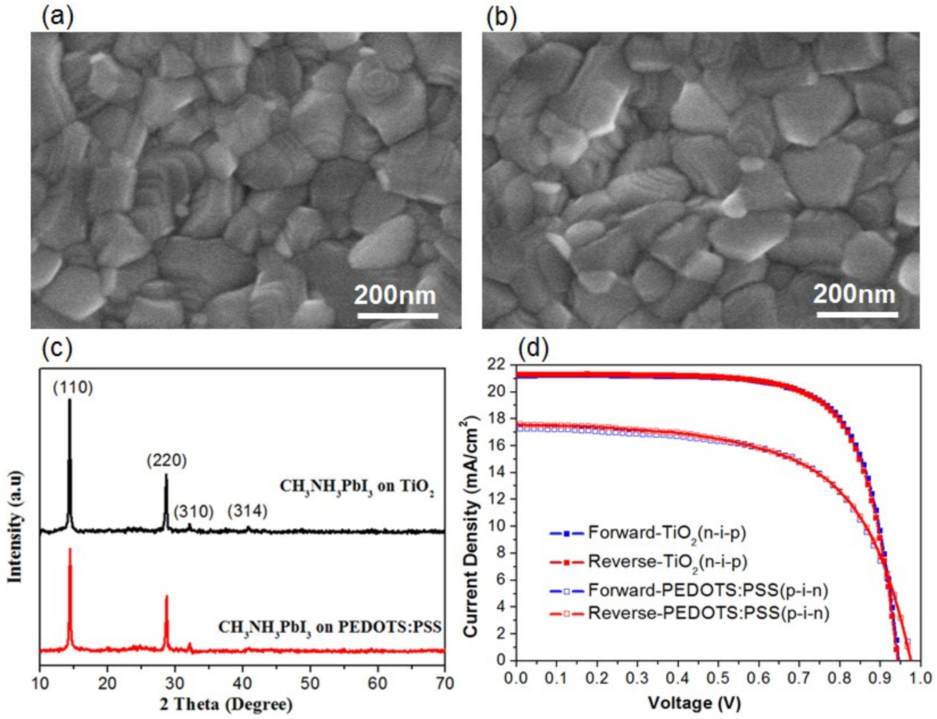

Fig. S1 SEM images of $CH_3NH_3PbI_3$ film on (a) FTO/TiO_2 and (b) FTO/PEDOTS:PSS substrates; (c) XRD spectra of $CH_3NH_3PbI_3$ on FTO/TiO_2 and FTO/PEDOTS:PSS substrates; and (d) J-V curves under forward (blue) and reverse (red) scans for FTO/TiO_2-based n-i-p (solid square) and FTO/PEDOTS:PSS-based p-i-n (hollow square) solar cells.

Table S1 Photovoltaic properties of solar cells under forward and reverse scans.

Device type	Scan direction	V_{oc} (V)	J_{sc} (mA/cm^2)	FF	PCE
n-i-p (TiO_2)	Forward	0.94	21.3	72.6%	14.5%
	Reverse	0.94	21.2	73.3%	14.6%
p-i-n (PEDOTS:PSS)	Forward	0.98	17.4	60.7%	10.3%
	Reverse	0.98	17.1	61.7%	10.4%

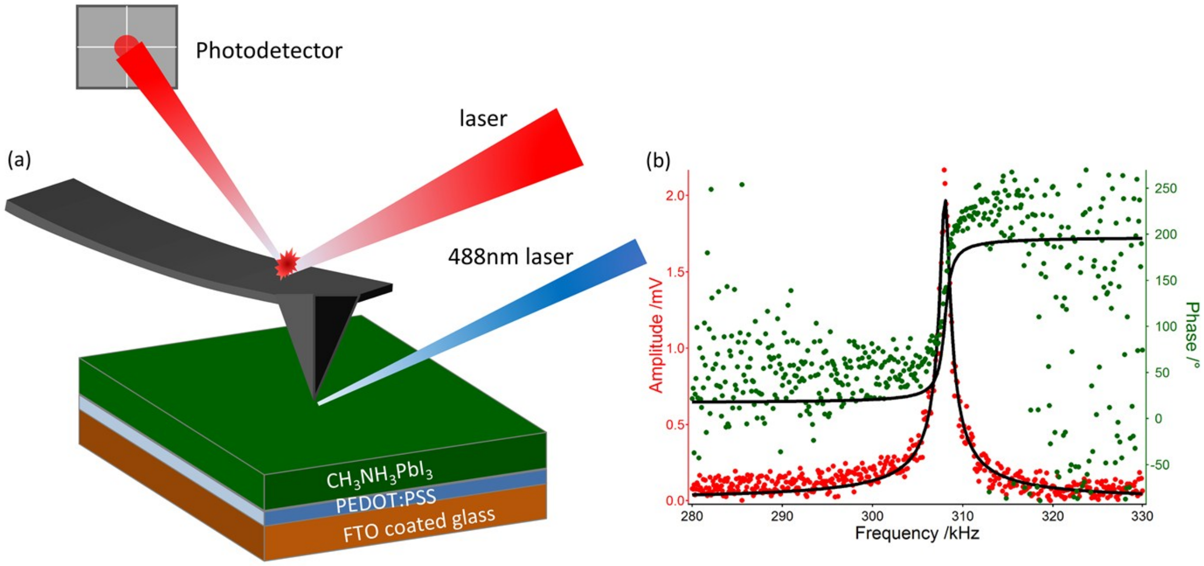

Fig. S2 (a) Schematic illustration of PFM experiment with optional light illumination; (b) piezoresponse as a function of applied frequency, showing resonance frequency at ω_0.

Piezoresponse force microscopy (PFM). The schematic of PFM under optional light illumination is shown in Fig. S2(a), wherein local piezoelectric displacement of the sample is measured by a laser photodiode system. In order to study the effect of light on the piezoresponse, a commercial blue LED with 488nm-wavelength was used to illuminate the top side of the sample. For PFM mapping, an AC voltage of 1V was applied through the conductive probe near the sample-probe resonance frequency ω_0 to enhance the sensitivity, as shown in Fig. S2(b), and the resonance frequency was tracked using dual-amplitude resonance tracking (DART) technique[3]. This yields the first harmonic PFM response, and in order to get the second harmonic response for nonlinear behavior, the excitation voltage is applied at $\omega_0/2$ yet the displacement is measured at ω_0, as schematically shown in Fig. S3. In this sketch, the blue boxes indicate a band of frequency range that is applied to excite the sample, centered at ω_0 or $1/2\omega_0$, while red blocks indicate the corresponding response measured at different frequencies, centered at ω_0.

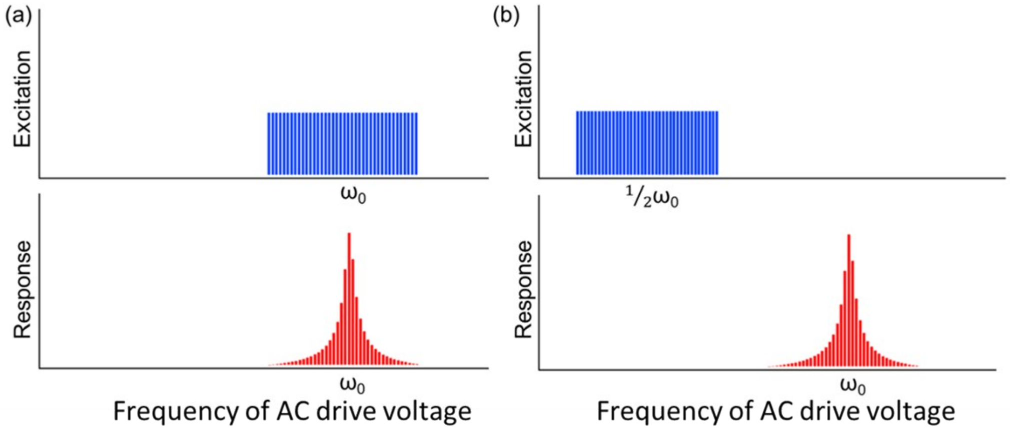

Fig. S3 Schematics of the first (a) and the second (b) harmonic PFM response measurements.

It is important to recognize that in a standard PFM experiment, only first harmonic response is measured, which only probes linear effect, and thus the response is by definition linear with respect to the AC voltage applied for any systems, regardless of their microscopic mechanisms and nonlinearity. To elaborate this important yet subtle point, let AC voltage be

$$V = V_0 e^{i\varpi t}\,, \tag{1}$$

where ω is the excitation frequency, and assume that the electromechanical response of the sample has both linear and quadratic contributions:

$$A = dV + QV^2\,. \tag{2}$$

Then it is seen from Eqs. (1) and (2) that

$$A = dV_0 e^{iwt} + QV_0^2 e^{i2wt}\,. \tag{3}$$

Clearly, the first harmonic response amplitude dV_0 is linear to the applied AC voltage, as exhibited in Fig. S4, even if the system has large nonlinear effect. It reveals nothing about nonlinear behavior though, and thus cannot tell us whether linear or nonlinear response dominates in the system. To answer this question, it is necessary to compare the first and second harmonic responses, and we developed second harmonic PFM technique in our lab to probe possible nonlinear behavior in piezoresponse [4], as shown by Fig. S3(b).

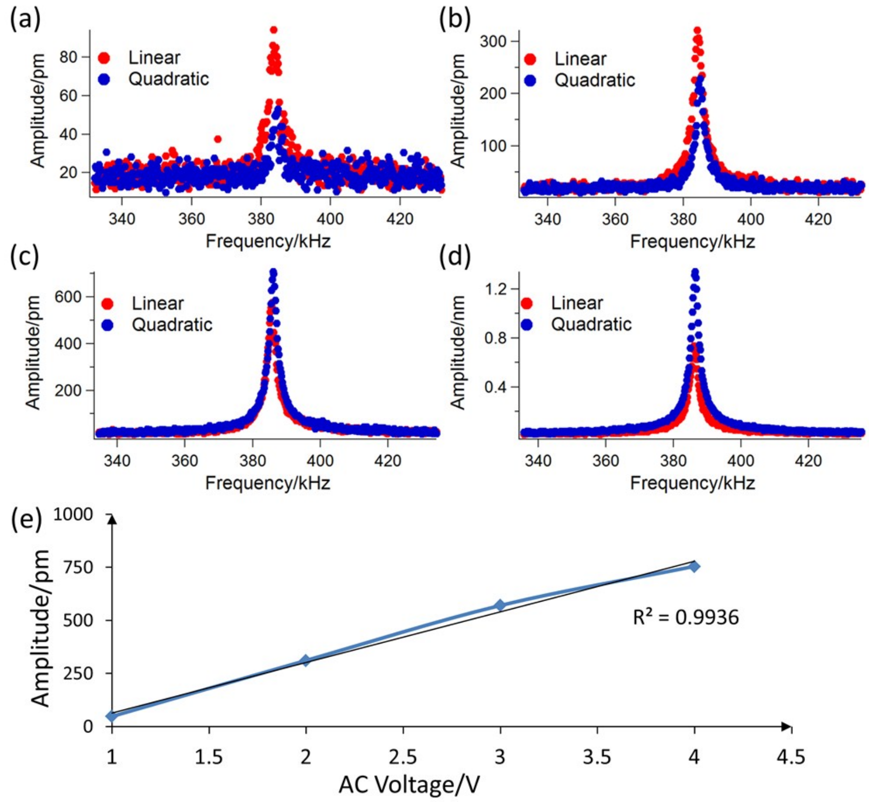

Fig. S4 (a-d) The first and second harmonic PFM responses of $CH_3NH_3PbI_3$ film on FTO/PEDOTS:PSS substrate under 1, 2, 3, and 4V AC excitation, showing prominent nonlinear effect in the system; and (e) the first harmonic response versus AC voltage applied, showing linear relationship between first harmonic response and the AC voltage, despite large nonlinear effect existing in the system.

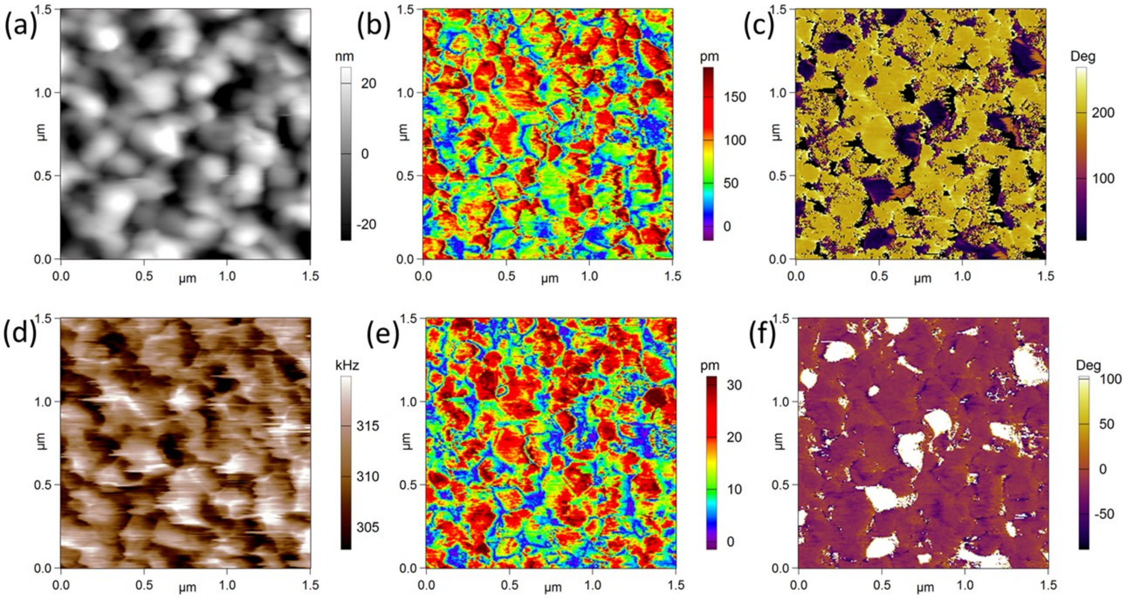

Fig. S5 Original DART mappings of Fig. 1, before corrected by damped driven harmonic oscillator model; (a) topography, (d) resonance frequency, (b) amplitude and (c) phase on the left side of resonance, and amplitude (e) and phase (f) on the right side of the resonance.

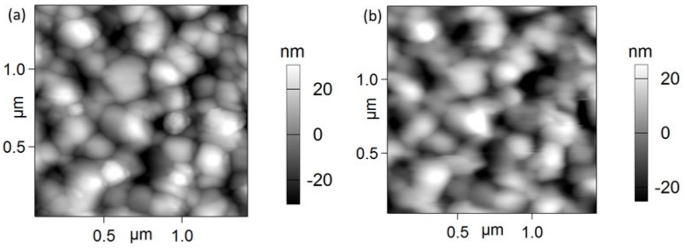

Fig. S6 Topography mapping of Fig. 1 from (a) tapping mode and (b) contact mode.

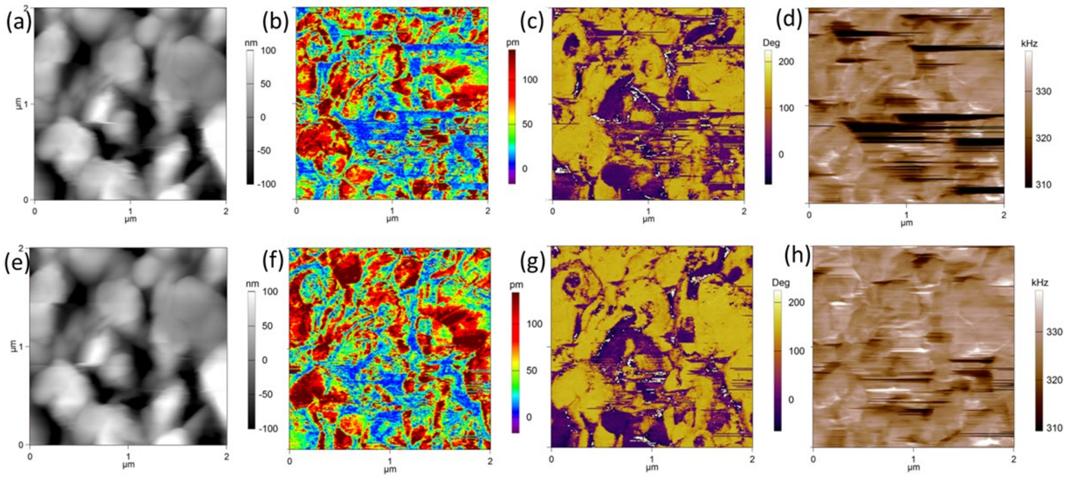

Fig. S7 PFM trace (top row) and retrace (bottom row) mapping of $CH_3NH_3PbI_3$ film on FTO/PEDOTS:PSS substrate at room temperature, including mappings of topography (ae), PFM amplitude (bf), phase (cg), and resonant frequency (dh).

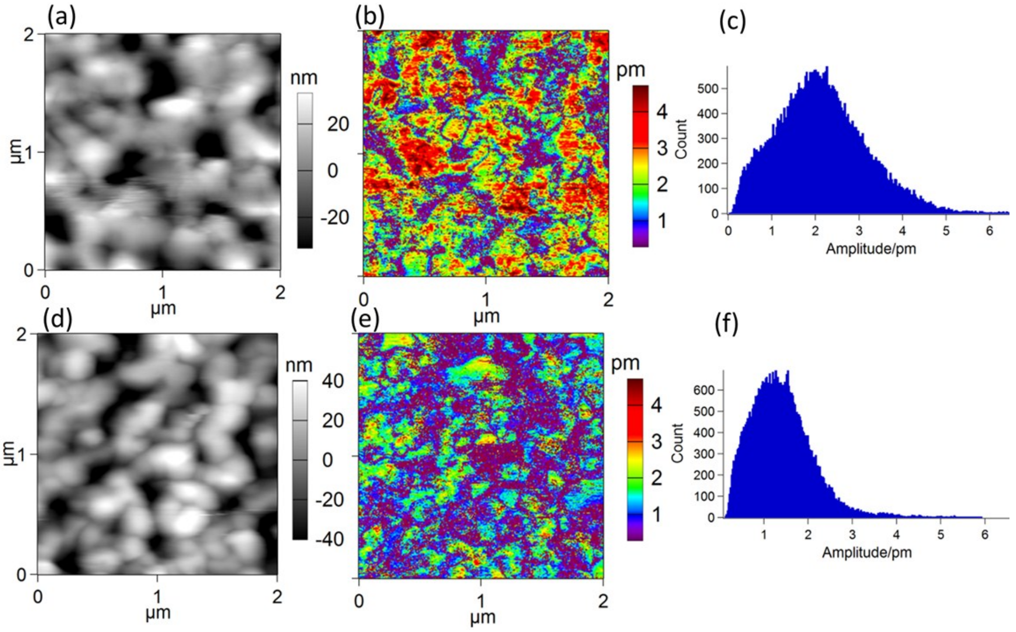

Fig. S8 Comparison of PFM mapping of $CH_3NH_3PbI_3$ film on FTO/PEDOTS:PSS substrate at room temperature (top row) and 50°C (bottom row), including mappings of topography (ad) PFM amplitude (be), and corresponding histogram distribution of PFM amplitude (cf).

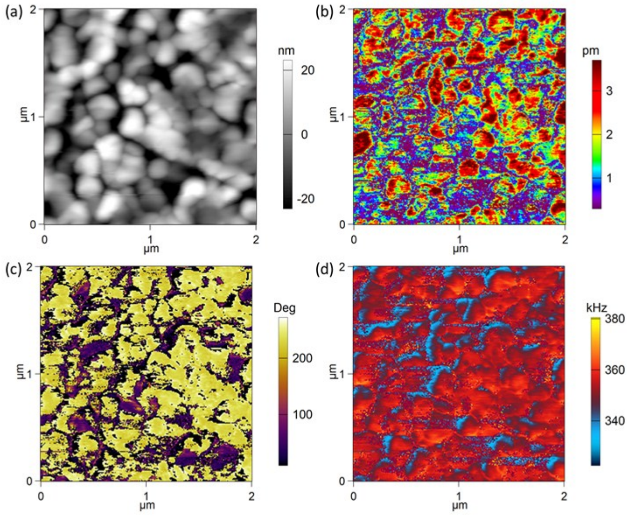

Fig. S9 DART-corrected (a) topography, (b) PFM amplitude, (c) phase and (d) frequency mappings of $CH_3NH_3PbI_3$ film on FTO/TiO_2 substrate.

Kelvin probe force microscopy (KPFM). For KPFM measurements, the probe scans the surface topography using tapping mode first and a 1V AC voltage was applied on the probe near its resonance frequency (~75kHz) to measure the sample surface potential distribution through a DC voltage feedback loop. All KPFM mappings were performed at a lift height of 0.5nm and a 3V DC voltage was applied to the probe. Each mapping takes about 10min. Note that on the same location, the surface potential is stable with respect to time, varying by only a few mV, as shown in Figs. S11 and S12.

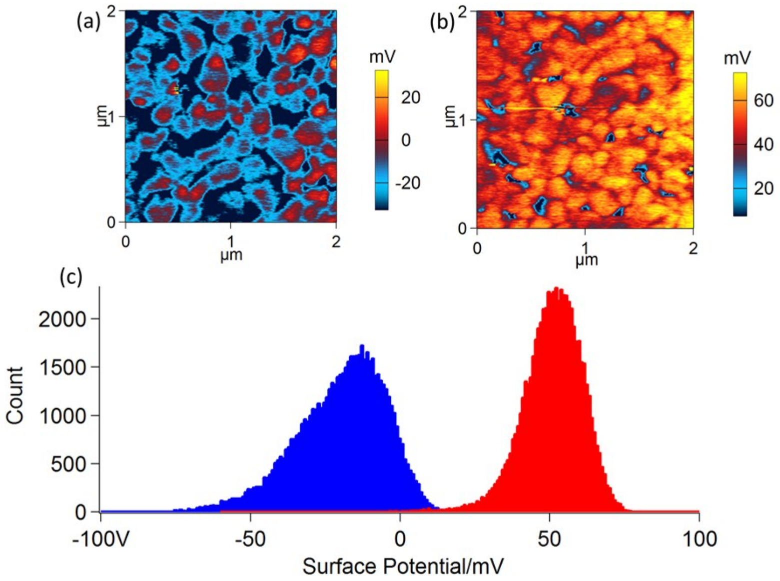

Fig. S10 Different surface potential distribution of $CH_3NH_3PbI_3$ film on FTO/TiO_2 substrate, (a) and (b) are KPFM surface potential mappings of the film at different locations, and (c) is corresponding histogram distribution of surface potential.

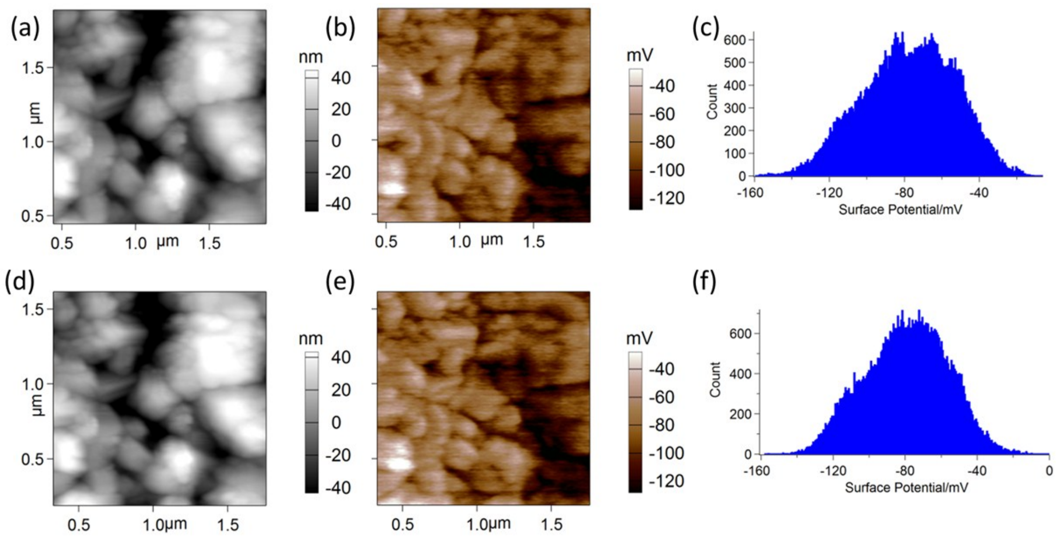

Fig. S11 Initial mapping (top row) and mapping after 20 minutes (bottom row) show stability of surface potential measured for $CH_3NH_3PbI_3$ film on FTO/PEDOTS:PSS substrate in dark with respect to time; (ad) topography; (be) surface potential; (cf) histogram of surface potential.

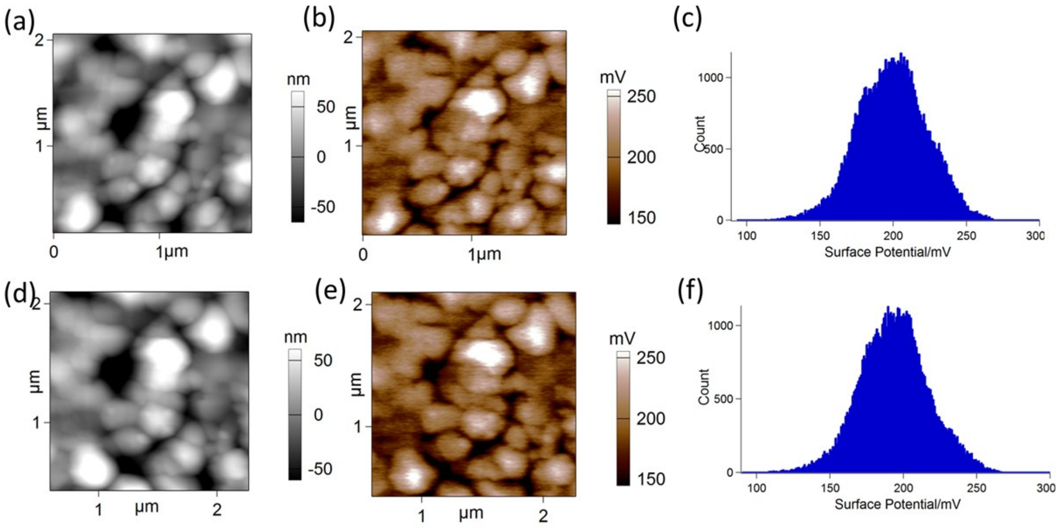

Fig. S12 Initial mapping (top row) and mapping after 20 minutes (bottom row) show stability of surface potential measured for $CH_3NH_3PbI_3$ film on FTO/TiO_2 substrate in dark with respect to time; (ad) topography; (be) surface potential; (cf) histogram of surface potential.

In addition, the sample was exposed to the 488 nm-wavelength light illumination, chosen according to UV-Vis spectra of $CH_3NH_3PbI_3$ film shown in Fig. S13, for at least 1min before doing the KPFM mapping, such that there is enough time for the photo-induced charge transport, and the surface potential shift due to light illumination is evident, as shown in Figs. S14 - S16. The current mappings measured in dark, under light illumination, and then in dark are shown in Fig. S17.

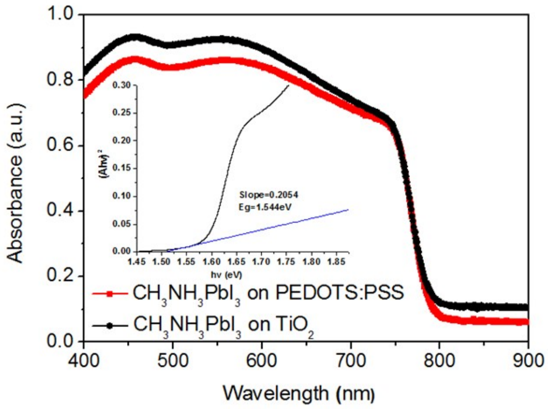

Fig. S13 UV-vis absorption spectra of $CH_3NH_3PbI_3$ film on FTO/PEDOTS:PSS substrate and FTO/TiO_2 substrate, the inset plots $(Ah\nu)^2$ with respect to the photon energy ($h\nu$) for $CH_3NH_3PbI_3$ film.

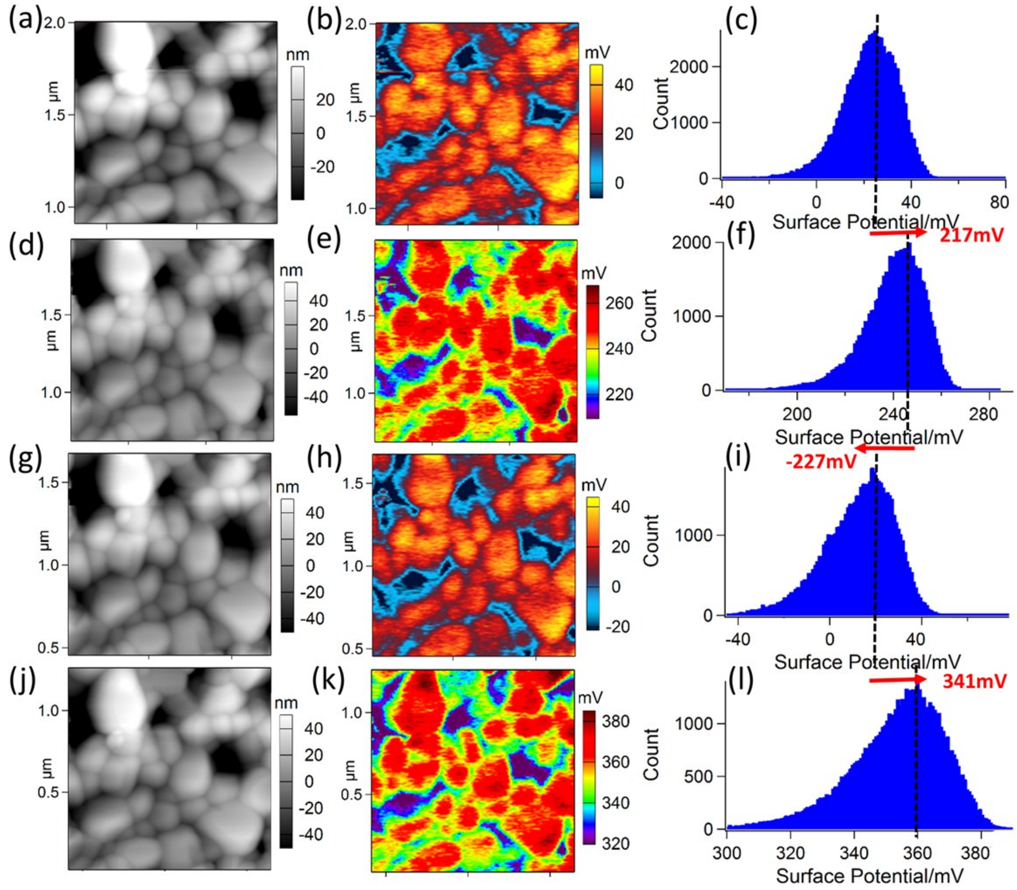

Fig. S14 Surface potential change of $CH_3NH_3PbI_3$ film on FTO/TiO_2 substrate induced by light illumination with 488nm-wavelength laser; (a), (d), (g) and (j) are topography showing the same region for comparison, (b), (e), (h) and (k) are surface potential mappings, and (c), (f), (i) and (l) are corresponding histogram distributions, showing positive shifting of surface potential under light illumination; first row was measured in dark, and second row measured under light illumination, followed by measuring in dark again, shown in the third row, and finally, last row was measured under light illumination again.

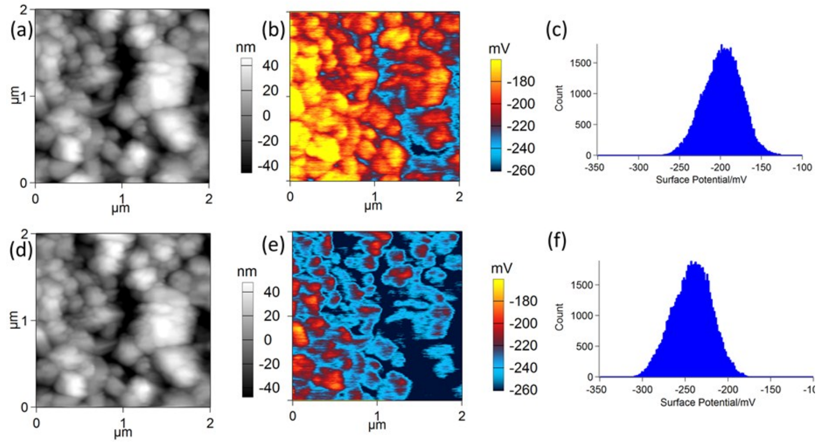

Fig. S15 Reduction of surface potential under light illumination for 15min measured for $CH_3NH_3PbI_3$ film on FTO/PEDOTS:PSS substrate; (ad) topography; (be) surface potential; (cf) histogram of surface potential.

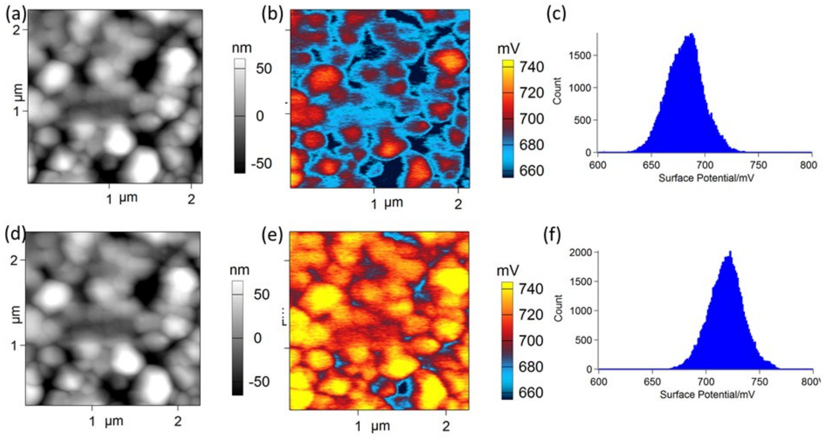

Fig. S16 Increase of surface potential under light illumination for 15min measured for $CH_3NH_3PbI_3$ film on FTO/TiO_2 substrate; (ad) topography; (be) surface potential; (cf) histogram of surface potential.

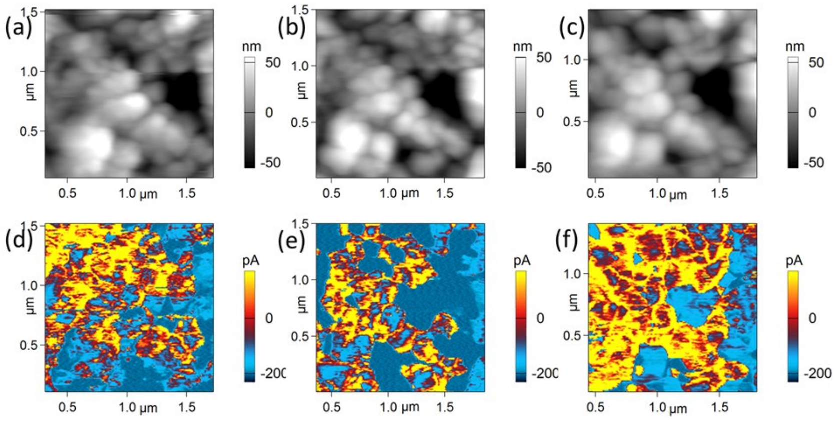

Fig. S17 Current mapping in dark and under illumination of $CH_3NH_3PbI_3$ film on FTO/PEDOTS:PSS substrate, (a), (b) and (c) are topography showing the same region for comparison, (d), (e) and (f) are corresponding current distribution under light illumination, in dark and then under light illumination again; 2V DC voltage is applied to the sample surface for current measurement.

PFM switching. The PFM hysteresis loops were measured with two cycles of DC voltage in an overall triangle form applied to the probe, with the stepwise increasing DC voltage alternating between on and off states, as schematically illustrated in Fig. S18(a). On top of the DC voltage, there is a small AC voltage imposed to excite the piezoresponse, from which the DC voltage-induced polarization switching can be detected from the phase reversal. Here, we varied the maximum value of DC voltage and the period of each DC voltage cycle to study their effects on the PFM hysteresis. PFM amplitude butterfly and phase hysteresis loops measured under different periods of each DC voltage cycle are presented in Fig. S18(b,c), showing insensitivity of coercivity to the rate of DC voltage applied. Similar switching characteristics is observe in $CH_3NH_3PbI_3$ film on FTO/TiO_2 substrate, as shown in Fig. S19.

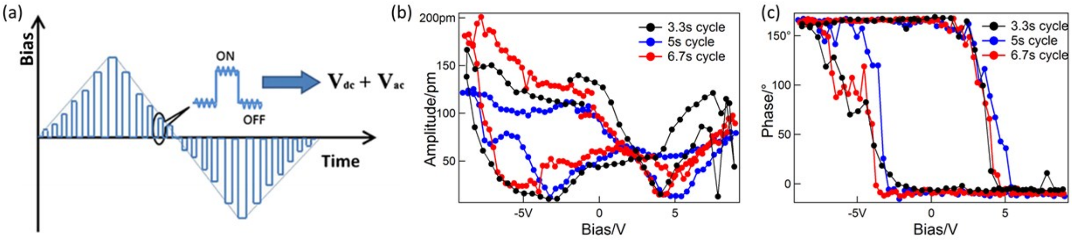

Fig. S18 (a) Schematic of the voltage signal applied during the PFM switching measurement; and PFM switching of $CH_3NH_3PbI_3$ film on FTO/PEDOTS:PSS substrate under different rate of DC voltage applied: (b) butterfly loop and (c) hysteresis loop.

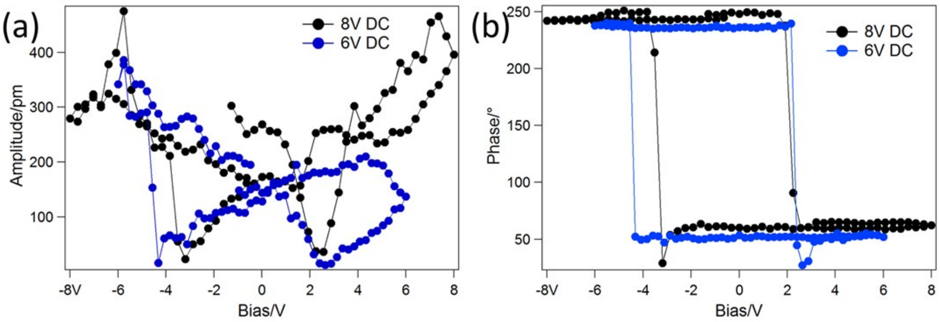

Fig. S19 PFM switching of $CH_3NH_3PbI_3$ film on FTO/TiO_2 substrate under different max DC biases; (a) butterfly loop and (b) hysteresis loop.

Photo-induced PFM switching. Photo-induced PFM switching is also observed in $CH_3NH_3PbI_3$ film on FTO/TiO_2, as shown in Fig. S20. But reversal of PFM phases and reduction in piezoresponse were not always observed. As shown in Fig. S21, the mappings of topography, PFM amplitude and phase, as well as the histogram distribution of piezoresponse remain unchanged before and after light illumination. The light illumination does affect the electric field-induced ferroelectric switching characteristics though, as shown in Fig. S22.

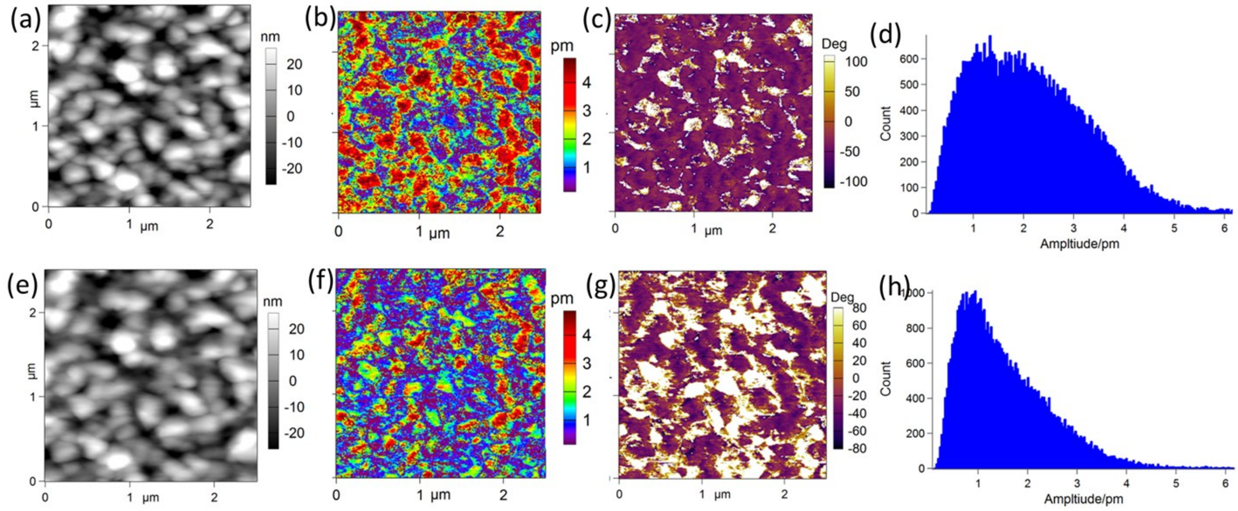

Fig. S20 PFM mappings of $CH_3NH_3PbI_3$ film on FTO/TiO_2 in dark (top row) and under light illumination (bottom row), showing clear photo-switching and reduction of PFM amplitude. The top row gives mappings of topography (a), PFM amplitude (b), and phase (c) measured in dark, while the bottom row gives corresponding mappings under illumination of 488 nm-wavelength laser, in the same region as indicated by topography; the comparison of histogram distribution of PFM in dark (d) and under illumination (h) is also given.

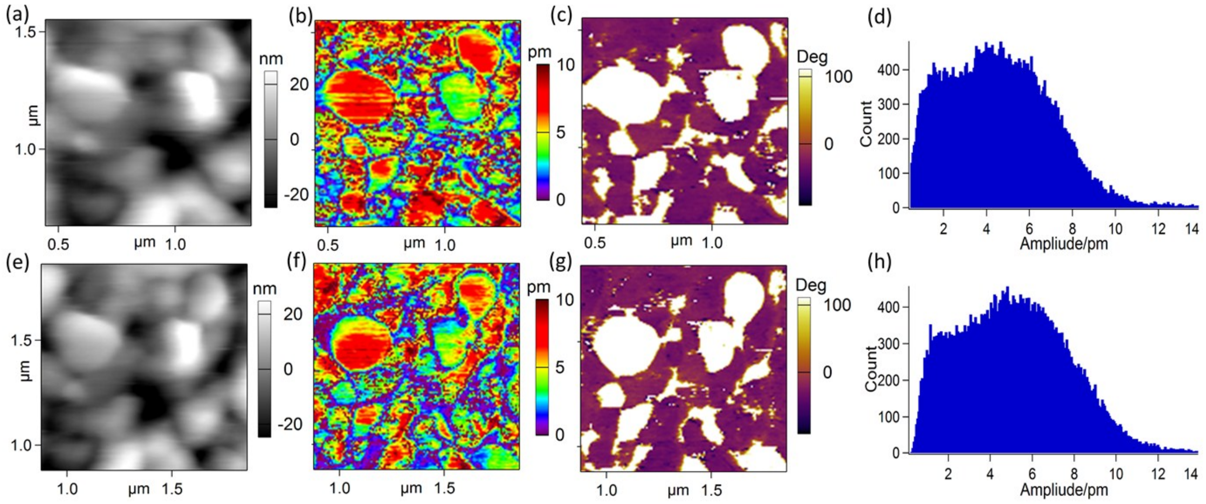

Fig. S21 Comparison of PFM mapping of $CH_3NH_3PbI_3$ film on FTO/PEDOTS:PSS substrate in dark and under illumination; the top row gives mappings of topography (a), PFM amplitude (b), and phase (c) measured in dark, while the bottom row gives corresponding mappings under illumination of 488 nm laser, in the same region as indicated by topography; the comparison of histogram distribution of PFM in dark (d) and under illumination (h) is also given.

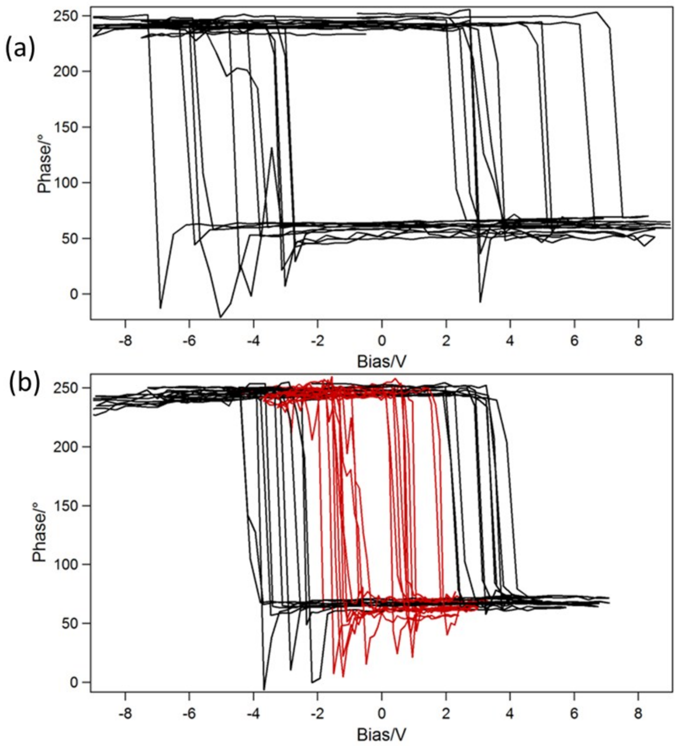

Fig. S22 The effect of light illumination on ferroelectric switching characteristics of $CH_3NH_3PbI_3$ film deposited on FTO/TiO_2 substrate; (a) PFM hysteresis loops measured in dark and (b) PFM hysteresis loops measured under light illumination. The loops are centralized with respect to bias to illustrate the reduction of coercivity induced by light illumination.

References

1. Q. Chen, H. Zhou, Z. Hong, S. Luo, H.-S. Duan, H.-H. Wang, Y. Liu, G. Li and Y. Yang, *J. Am. Chem. Soc.,*2014, **136**, 622-625.
2. J. Burschka, N. Pellet, S.-J. Moon, R. Humphry-Baker, P. Gao, M. K. Nazeeruddin and M. Grätzel, *Nature,* 2013, **499**, 316-319.
3. B. J. Rodriguez, C. Callahan, S. V. Kalinin and R. Proksch, *Nanotechnology,* 2007, **18**, 475504.
4. Q. N. Chen, Y. Ou, F. Ma and J. Li, *Appl. Phys. Lett.,* 2014, **104**, 242907.